6

Ferroelectric and Multiferroic Class of Perovskite Oxides and their Rubber Composites for 8-18 GHz MW Absorption

6.1 INTRODUCTION

Microwave absorbing properties of ABO_3 type perovskite oxides e.g. $LaNiO_3$, $La_{1-x}Ca_xMnO_3$, $PbTiO_3$ etc. are being explored widely due to their high permittivity values at GHz frequencies, better impedance matching and synergetic contribution of complex permittivity and permeability values [Liu *et al*., 2003; Li *et al*., 2009; Jiang *et al.,* 2014]. However, it is challenging to tune their dielectric and magnetic properties for MW absorption in the desired frequency range. Further, the synthesis of pure phase material with re-producible physical properties is often more difficult and especially the large scale production of these materials with enhanced yields. These materials are not much studied earlier for their MW absorption properties. In this chapter, we have focused on synthesis of both $BaTiO_3$ ferroelectric and $BiFeO_3$ multiferroic materials using novel synthesis methods and their MW absorption properties are explored in rubber based composites for possible microwave applications.

6.2 DEVELOPMENT OF TETRAGONAL BARIUM TITANATE ($BaTiO_3$) FERROELECTRICS AND ITS RUBBER COMPOSITES

Ferroelectric materials exhibit spontaneous polarization, which can be altered by modulating external electric field. In addition, these materials also show high value of dielectric constant and constant permeability values over broad MW frequency range [Hench and West, 1989; Verma *et al*., 2003]. The onset of ferroelectricity in these materials is due to the formation of ferroelectric domains and their alignment under applied electrical field. The overall polarization in ferroelectric materials is primarily contributed by electrical/dipolar polarization originated by atomic ordering of ions at the crystal sites. These materials attenuate the MW signal by dipole relaxation due to orientation lagging of these diploes with respect to the external electric field vector ($\vec{E}$). The most common ferroelectric material, barium titanate ($BaTiO_3$), is widely studied for its dielectric and piezoelectric properties and utilized extensively in variety of applications viz. Multi-layer Ceramic Capacitors (MLCs), Ferroelectric Random Access Memory (FRAMs), transducers, thermistors etc. [Jaffe *et al*., 1971; Vijatovic *et al*., 2008; Ertug, 2013]. $BaTiO_3$ has been mostly explored in kHz-MHz frequency range for such applications, and very few reports are available on dielectric studies of this material at GHz region. This material shows ferroelectric properties at T< 120°C in tetragonal crystallographic phase and above this temperature, it changes into cubic structure, which is paraelectric in nature. The crystal structure of $BaTiO_3$ is shown in Figure 6.1(a), wherein Ba^{2+} cations are crystallographically located at eightfold sites of the unit cell in (0 0 0) position, Ti^{4+} ion at (½, ½, ½) position and the rest positions are occupied by oxygen anion. In the ferroelectric phase, $BaTiO_3$ converts into tetragonal phase with space group of P4mm, by slight off-center shifting of Ti^{4+} ion within TiO_6 octahedral arrangement along <100> direction [Jaynes, 1953; Rabe, 2007]. This displacement of Ti^{4+} ion in the tetragonal crystal lattice, gives rise to the net permanent polarization along c-axis. Under the influence of external MW radiation, the direction of off-centric displacement of Ti^{4+} ion may change to up and down

positions, following external electric field, leading to the MW absorption by relaxing these dipoles, as schematically shown in Figures 6.1(a)-(c). The strength of ferroelectricity in the $BaTiO_3$ material is estimated by the tetragonality (c/a) ratio, which represents the respective distortion from its high temperature cubic phase, where the length of c-axis gets elongated (~1.011) because of preferred distortions, as explained in earlier studies [Strukov, 1998; Cohen, 1992].

Recently, dipolar relaxation mechanism in ferroelectric $BaTiO_3$ is being explored immensely to identify its MW absorbing properties because of its large ferroelectric polarization and material's stability for any practical application [Chen *et al.*, 2007]. However, the main constraint lies in the designing materials with high degree of off-centrosymmetric Ti-O bond in TiO_6 octahedral in the $BaTiO_3$ crystal lattice without losing ferroelectric properties. However, the degree of non-centro symmetry of Ti^{4+} ion in $BaTiO_3$ system depends strongly on the synthesis methods and its processing conditions, which is the genesis of ferroelectricity and thus, microwave absorption properties [Murugan *et al.*, 2010].

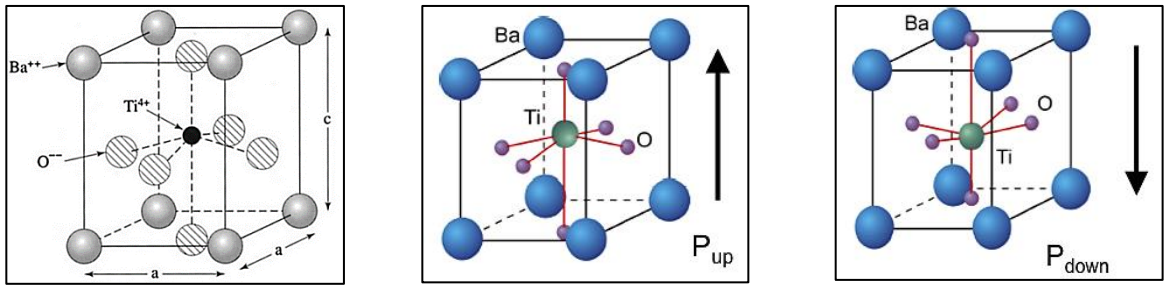

Figure 6.1 (a) Crystal structure of tetragonal $BaTiO_3$, (b)-(c) Polarization in $BaTiO_3$ due to displacement of Ti^{4+} ions

Efforts have been made in recent years to prepare tetragonal $BaTiO_3$ by utilizing various synthetic methods such as Microwave Assisted Hydrothermal Synthesis (MAHS) [Lu *et al.*, 2000; Nyutu *et al.*, 2008], sol-gel process [Cernea *et al.*, 2005], Low Temperature Aqueous Synthesis (LTAS) [Zhigang *et al.*, 2006], solid state route [Manzoor and Kim, 2007; Pavlovic *et al.*, 2008] etc. Further, their composites have also been made with paraffin wax [Zhu *et al.*, 2012], epoxy [Jain *et al.*, 2013] etc. to investigate MW absorption properties in different frequency bands. It has been observed that EM dispersion characteristics of these composite materials strongly depend on the percentage of loading and their distribution in the host matrices. Further, the filler-matrix interactions within the composites also play an important role in deciding the microwave absorption behavior. Although, $BaTiO_3$ is a widely studied material at radio frequencies, there are limited studies on MW absorption for its composite systems. Thus, it will be interesting to explore its properties at MW frequencies, particularly for its rubber/polymer composite matrix based systems for possible practical applications.

In the present study, a simple, scalable and energy efficient solid state processing route is reported for the preparation of phase pure $BaTiO_3$ powder with enhanced tetragonality. The synthesized powder has been annealed at different elevated temperatures to study their size-dependent physical and microwave properties. Flexible sheets have been fabricated with different loadings of identified $BaTiO_3$ powder in NBR rubber matrix. Reflection losses have been estimated for the prepared $BaTiO_3$/NBR composite sheets at different thicknesses in 8 – 12 GHz frequency range.

6.2.1 Experimental Procedure

Tetragonal $BaTiO_3$ powder was synthesized by using solid- state reaction of mechanically activated $BaCO_3$-TiO_2 system. $BaCO_3$ (Across 99+%) powder was milled using analytical mill (Make: IKA) at 20,000 RPM for 15 minutes for its mechanical activation. Equi-molar mixtures of mechanically activated $BaCO_3$ and TiO_2 (P25 Degussa) powders were homogenized by milling for 10 minutes at 10,000 RPM in an analytical mill. The solid mixture was annealed at 700°C,

900°C, 1000°C and 1100°C temperatures at 12°C/min heating rate for 4h in air ambiance and their microwave absorption properties are investigated. The synthesized $BaTiO_3$ powder, with optimal MW absorption properties, was selected as a filler material in NBR matrix. Rubber based microwave absorbing sheets were fabricated with the help of Two Roll Mixing Mill (TRMM) and High-Temperature Compression Moulding Press (HTCMP). Initially, 50 gm of NBR was thoroughly mixed into Mill and $BaTiO_3$ powder was added in different filler ratios as listed in Table-6.1. These synthesis steps for tetragonal $BaTiO_3$ phase powder and its rubber based composite sheets are schematically shown in Figure 6.2.

Structural, chemical, and morphological characterizations are carried out using X-Ray Diffraction (XRD), Fourier Transmission Infra-Red Spectroscopy (FTIR) and Scanning Electron Microscopy (SEM) techniques. The Raman Spectroscopy measurements have been carried out to investigate the tetragonal character of the synthesized powder samples. Further, Vector Network Analyzer (VNA) has been used to compute complex permittivity, permeability and tangent losses in X (8.2-12.4 GHz) and Ku (12.4-18 GHz) MW frequency bands.

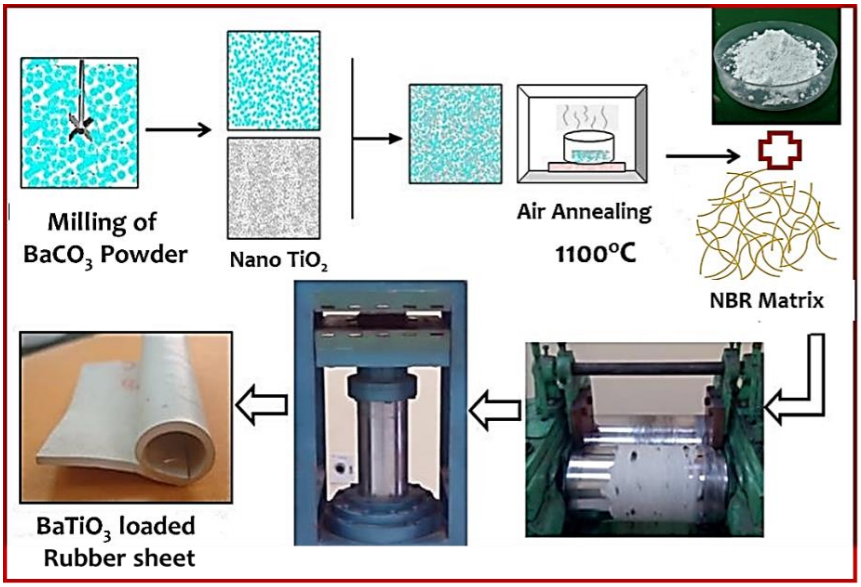

Figure 6.2 : (a) Schematic for solid state synthesis of tetragonal $BaTiO_3$ powder and fabrication of rubber based composites

Table 6.1: List of tetragonal $BaTiO_3$ powder loaded rubber composites

S. No.	Sample Code	Quantity of NBR (g)	Wt% of $BaTiO_3$ in compound	Quantity of $BaTiO_3$ Powder (g)	Enhancement in filler loading as compared to sample MWAR50 (x)
1	MWAR50	50	50	50	1
2	MWAR60	50	60	75	1.5
3	MWAR70	50	70	116.7	2.33
4	MWAR80	50	80	200	4

6.2.2 Results and Discussions

6.2.2.1 X-ray Diffraction Analysis

XRD spectra of $BaTiO_3$ powder samples are plotted in Figure 6.3 (a). These measurements suggest that 700°C annealed powder sample consist of unreacted $BaCO_3$ in syntheiszed $BaTiO_3$ material. However, samples annealed at 900°C and 1000°°C showed phase pure $BaTiO_3$ without any residual impurities and the existence of (002) and (200) crystal planes near 2θ ~45° suggest

the onset of tetragonality in $BaTiO_3$, consistent with reported work [Lee *et al.*, 2012]. The peaks near 2θ ~45° are further resolved with enhanced intensity for 1100°C annealed $BaTiO_3$ powder sample, as evident from the top panel of Figure 6.3(a). The lattice parameters 'a' and 'c' of the tetragonal $BaTiO_3$ structure are estimated from measured XRD spectra and the c/a ratio, has been calculated and plotted against annealing temperature in Figure 6.3(b). The tetragonality ratio has increased with annealing temperature and maximum ratio ~ 1.016 has been observed for 1100°C annealed $BaTiO_3$ sample, which is higher than earlier reported values [Strukov, 1998], suggesting the maximum distortion in tetragonal $BaTiO_3$ structure as compared to its ideal cubic structure.

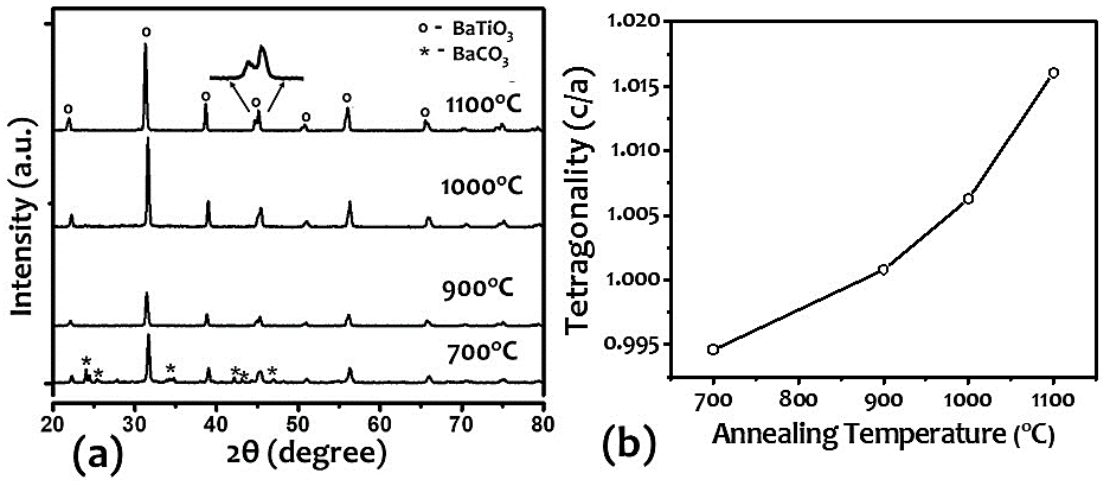

Figure 6.3 : (a) XRD pattern of $BaTiO_3$ powder samples annealed at different elevated temperatures of 700°C, 900°C, 1000°C, and 1100°C (b) Variation of tetragonality ratio with annealing temperature

6.2.2.2 FTIR Studies

FTIR spectra of these powders were recorded to ascertain the presence of any other residual impurities like $BaCO_3$, TiO_2 or intermediate phases in powder samples as shown in Figure 6.4. FTIR spectra of 700°C annealed sample shows absorption band at ~1440 cm^{-1} due to C=O asymmetric stretching vibrations of residual carbonate ion (CO_3^{2-}) [Nyutu *et al.*, 2008]. Further, broad absorption peaks observed at 3450 cm^{-1} and 1646 cm^{-1} correspond to the stretching and bending modes of O-H vibrational modes from the water molecules, respectively. The intensity of these bands has reduced with higher calcination temperature due to the removal of hydroxide ions and the decomposition of carbonate ions, leading to the formation of impurities free $BaTiO_3$ tetragonal phase. The characteristic absorption bands in the range of 537-600 cm^{-1} and 431-446 cm^{-1} are attributed to the formation of phase pure tetragonal $BaTiO_3$ perovskite structure [Kuruva *et al.*, 2013]. The strong band at ~600 cm^{-1} and weak band 446 cm^{-1} correspond to Ti-O vertical stretching vibration and O-Ti-O bending vibration of the TiO_6 octahedron in $BaTiO_3$ crystal lattice. These two bands are shifted systematically to lower wavenumbers with increasing the annealing temperature. This shift is attributed to the enhancement in particle size, dipolar interaction, and interfacial effects because of annealing at higher temperatures [Preudhomme and Tarte, 1971].

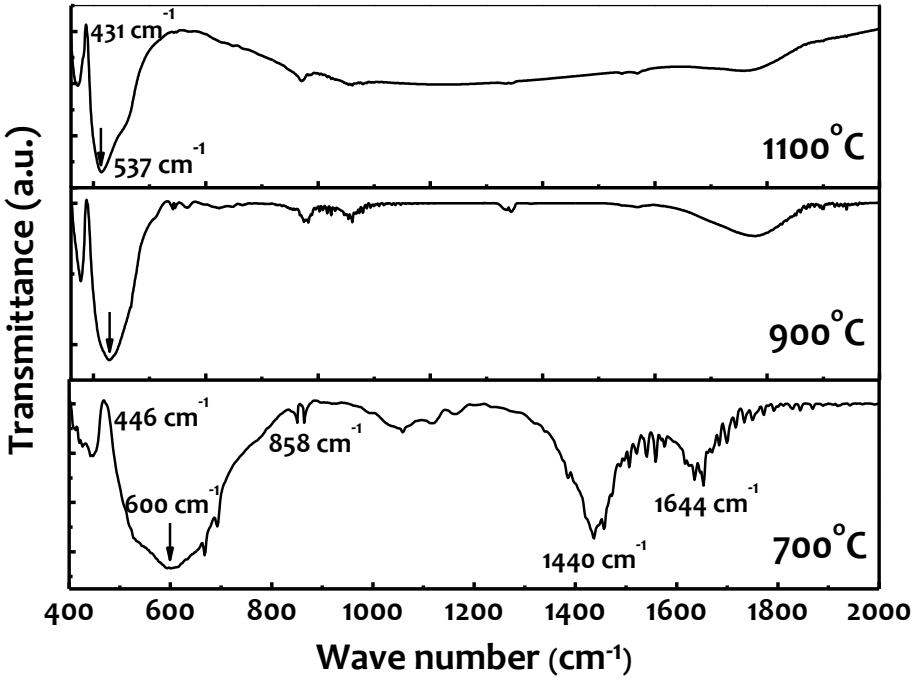

Figure 6.4 : FTIR pattern of $BaTiO_3$ powder samples annealed at different elevated temperatures of 700°C, 900°C, and 1100°C

6.2.2.3 Raman Studies

Raman spectroscopic measurements have been carried out on 700°C, 900°C, 1000°C and 1100°C annealed $BaTiO_3$ powder samples to probe the tetragonallity as a function of annealing temperature. This technique is highly sensitive to investigate the local atomic/molecular structure using the vibrational symmetry of $BaTiO_3$ system. Raman spectra of all these samples are shown in Figure 6.5 in 250-1000 cm^{-1} wavenumber range. The three vibrational modes at 310, 520 and 720 cm^{-1} are observed not only for samples annealed at 900°C, 1000°C and 1100°C, but also for the sample annealed at 700°C, however at relatively lower intensity. These bands are attributed to [B_1E (TO+LO)], [E_1A_1(TO)] and [A_1E (LO)] vibrational modes of tetragonal $BaTiO_3$ [Moreira *et al.*, 2008]. Further, enhancement of intensity for these vibrational modes with annealing temperature indicates the increase in tetragonality of $BaTiO_3$ samples with annealing temperature.

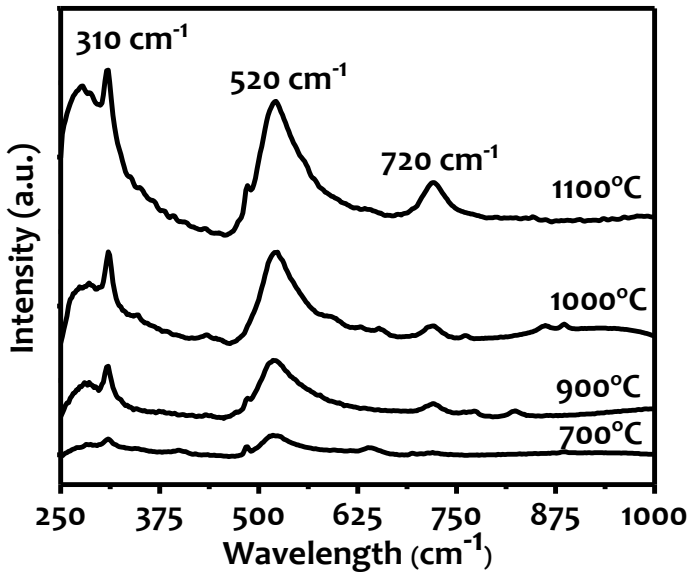

Figure 6.5 : Raman pattern of $BaTiO_3$ powder samples annealed at different elevated temperatures of 700°C, 900°C, 1000°C, and 1100°C

6.2.2.4 Morphological Studies

SEM micrographs of powders annealed at 700°C, 900°C, 1000°C and 1100°C are shown in Figure 6.6(a). $BaTiO_3$ powder annealed at 700°C shows fine microstructure with spherical particle morphology. The sample annealed at 900°C and 1000°C showed enhanced particle size with nearly spherical morphology. Further, the sample annealed at 1100°C showed irregular grains with wide particle size distribution, as shown in Figure 6.6a (iv). The corresponding EDX spectra confirm the presence of the stoichiometric ratio of Ba, Ti and O elements in all these annealed $BaTiO_3$ powder samples. A representative EDX spectra for $BaTiO_3$ powder annealed at 1100°C is shown in Figure 6.6(b).

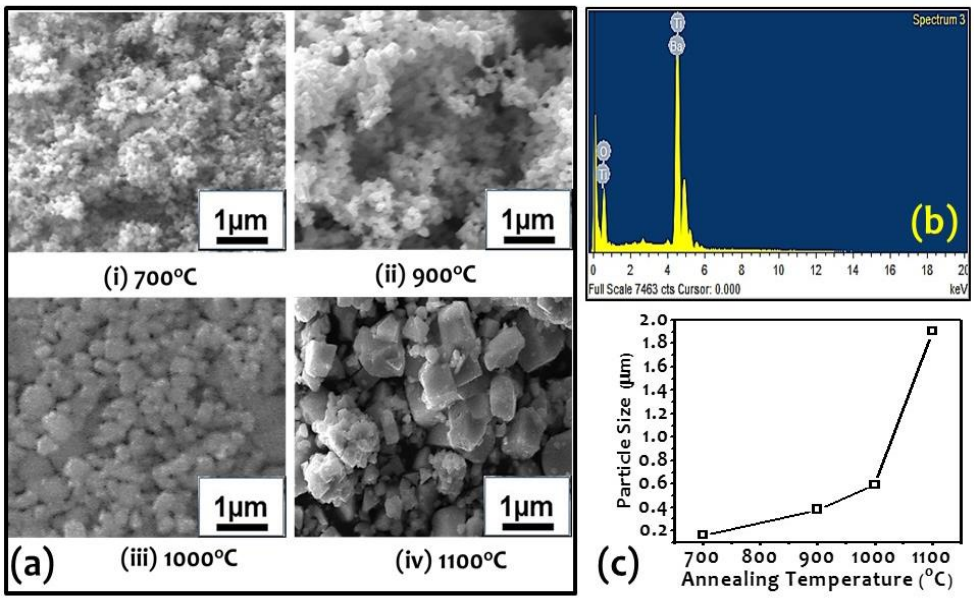

Figure 6.6 : SEM micrographs of $BaTiO_3$ powder samples annealed at different elevated temperatures of 700°C, 900°C, 1000°C, and 1100°C (b) Representative EDX spectra for $BaTiO_3$ powder sample annealed at 1100°C

The average particle size was determined using particle size analyzer for all these samples and results are shown in Figure 6.6(c). The particle size for $BaTiO_3$ powder annealed at 700°C is found ~160 nm, which has increased to ~380 nm and ~560 nm for 900°C and 1000°C annealed $BaTiO_3$ power samples, respectively. Finally, the particle size has increased up to ~1.9 μm for 1100°C annealed $BaTiO_3$ sample, which is in compliance with SEM studies. The observed increase in particle size has been attributed to the high temperature assisted grain growth.

6.2.2.5 Microwave Studies

The frequency dependent complex relative permittivity ($\varepsilon_r^* = \varepsilon_r' - j\varepsilon_r''$) and permeability ($\mu_r^* = \mu_r' - j\mu_r''$) plots are shown in Figure 6.7(a) for all these $BaTiO_3$ powder samples annealed at different annealing temperatures. The sample annealed at 700°C shows nearly frequency independent real permittivity values ~ 22.14 ± 1.2 over 8-18 GHz frequency range. A similar behavior has been observed for 900°C annealed sample, showing real permittivity values ~37.45 ± 2.95 over the investigated frequency range. However, the sample annealed at 1000°C starts showing frequency dependent real permittivity, which varies from 54 to 37 over 8-18 GHz frequency range. Further, the sample annealed at 1100°C shows enhanced real permittivity values ranging from ~73 to ~40 over 8-18 GHz frequency range. The imaginary part of the permittivity (ε_r'') of these materials is mainly responsible for the absorption of microwave energy inside the material. The sample annealed at 700°C shows ε_r'' values in the range of ~ -1.8 to -2.8. With increasing the annealing temperature up to 900°C the value of ε_r'' increased the range of ~ -4.0 to -6.5 over 8-18 GHz frequency range. Whereas the values of ε_r'' for the sample annealed at 1000°C shows variation in the range ~ -13 to -18 in this frequency range. Interestingly, the imaginary part of permittivity value for the 1100°C annealed sample shows large variation from ~-15 to -3.9 over the range with a broad minimum at ~ 11.5 GHz. The respective dispersion curves are summarized

in Fig. 6.7(a) bottom panel. The calculated loss tangent as a function of frequency is shown in Figure 6.7(b) over 8 - 18 GHz frequency range for all these different temperatures annealed samples. The $\tan\delta_e$ values for 700°C annealed samples are observed in the range of ~ -0.03 to -0.13, and for 900°C annealed samples, the values are found in the range of -0.10 to -0.21 over 8-18 GHz frequency range. Loss tangent values for the sample annealed at 1000°C, further increased and observed in the range of -0.22 to -0.37 over 8-18 GHz. The sample annealed at a higher temperature (1100°C) shows the highest negative values of loss tangent values ranging from -0.20 to -0.68 over 8-13.5 GHz frequency range and then nearly saturated afterward till 18 GHz. The real μ_r' and imaginary μ_r'' part of permeability values are ~1.0 and ~0.02 over the entire 8 - 18 GHz frequency range for all $BaTiO_3$ samples, thereby suggesting a negligible contribution of magnetic tangent loss in MW absorption for this material. This is also evident from the non-magnetic nature of $BaTiO_3$ material. Thus, these results suggest that the microwave absorption in $BaTiO_3$ powder is originating from dipolar relaxation within the material and no magnetic contribution is responsible for MW absorption. Microstructural parameters play a significant role in the dielectric and MW absorption performance of samples. Microstructurally, the powder annealed at 1100°C, is showing a wide distribution of large and irregular grain sizes as confirmed by SEM, Figure 6.6(a). This is even desired to realize the multiple scattering centers for the incident MW radiation within the absorber material and thus leading to enhanced MW absorption. XRD and Raman studies suggest that the tetragonal character of the synthesized $BaTiO_3$ powder increases with annealing temperature. The powder annealed at 1100°C showed the highest tetragonality due to the maximum displacement of Ti^{+4} ion against the negatively charged O^{-2} ions in TiO_6 octahedron in $BaTiO_3$ perovskite structure. This displacement leads to the creation of dipole moments, resulting into ferroelectric nature of $BaTiO_3$. The ferroelectric polarization strongly depends on the tetragonal nature of the pure $BaTiO_3$ sample. Further, on interaction with incident electromagnetic radiation, these dipoles in $BaTiO_3$ material, try to follow and align in the direction of external EM field by rotating the polarization vector along the field direction. The MW radiation loses its energy in the $BaTiO_3$ samples due to the dipolar relaxation process while following the external time varying electric field.

Among these different temperatures annealed $BaTiO_3$ bulk samples, 1100°C annealed $BaTiO_3$ bulk sample showed the maximum tetragonality and thus, the maximum spontaneous ferroelectric polarization, leading to the enhanced microwave absorption in this sample. Therefore, this 1100°C annealed $BaTiO_3$ powder has been selected for the preparation of rubber composites to understand the microwave absorption over the entire 8-18 GHz frequency range for possible applications.

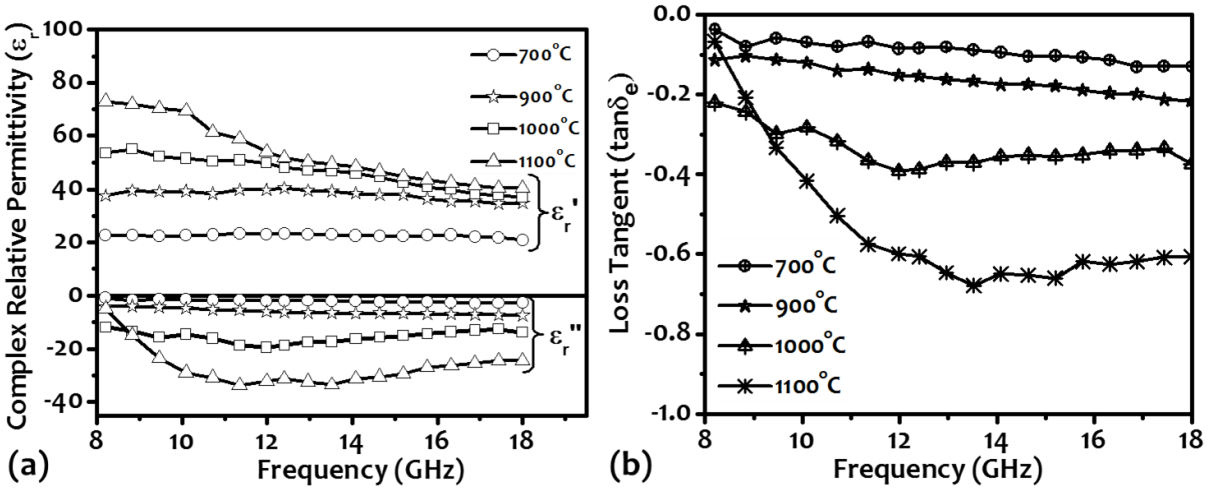

Figure 6.7: (a) Real and imaginary permittivity plots for annealed $BaTiO_3$ powders over 8-18 GHz frequency range (b) Dielectric loss tangent ($\tan\delta_e$) plots for respective powder samples

The detailed composite sample preparation and their physical studies are discussed by Saini *et al.* [Saini *et al.*, 2016]. In brief, the real permittivity, ε_r', dispersions are shown in Figure 6.8(a) for MWAR50, MWAR60, MWAR70 and MWAR80 $BaTiO_3$/NBR composite MW absorbers over 8 - 18 GHz frequency range. The real permittivity values are almost constant over the investigated frequency range for individual samples, however, the relative increase from 4 to 12 has been observed with increasing the $BaTiO_3$ loading fraction from 50 to 80wt% in NBR rubber matrix. Further, the imaginary part of relative permittivity ε_r'' has also increased from~ -0.1 to -0.65 with the $BaTiO_3$ loading fraction up to 80wt%, as shown in Figure 6.8(d). Measured real and imaginary permeability values were ~1 and 0.002 respectively for $BaTiO_3$/NBR composite samples in 8-18 GHz investigated frequency range, suggesting the significant contribution in MW absorption is coming only from permittivity dispersion for these composite materials.

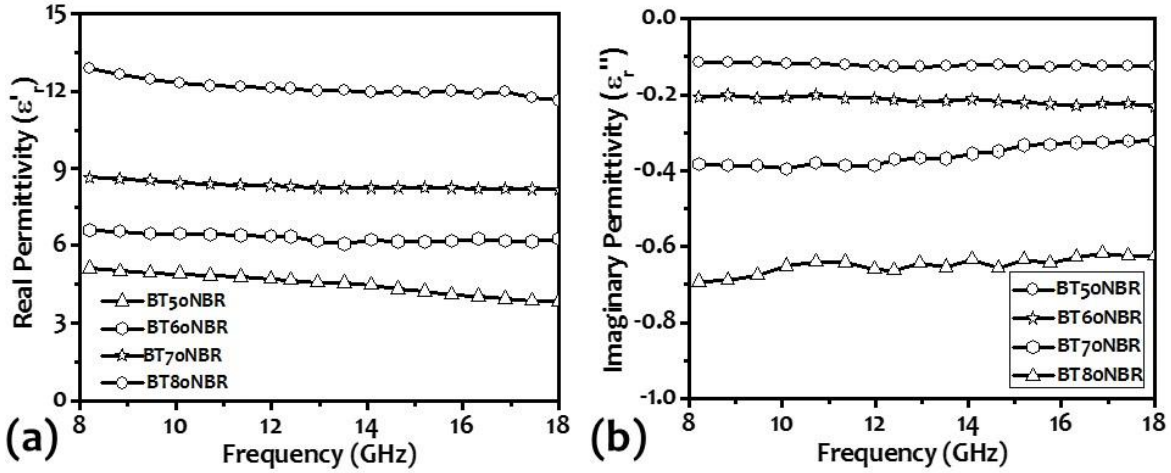

Figure 6.8 : (a) Real and (b) imaginary permittivity of $BaTiO_3$/NBR composite with different loading of $BaTiO_3$ powder annealed at 1100°C

The reflection loss (R.L.) values for pure NBR sheets are calculated for 6.5, 8, 9 and 10 mm thicknesses and results are shown in Figure 6.9(a). These measurements suggest extremely poor MW absorption properties due to the absence of MW lossy filler material in NBR rubber sheets. The maximum R.L. ~4 dB was observed at ~13 GHz for 10 mm thick pure NBR sheet. Further, the optimum R.L values of pure $BaTiO_3$ are also not very significant and even the maximum R.L. values were found ~ 7 dB for the optimized thickness of t=2.2 mm, as shown in Figure 6.9(b). The observed low values of R.L. for pure $BaTiO_3$ has been attributed to high impedance mismatch between air and pure $BaTiO_3$ absorber (Z~ 50Ω, as compared to free space impedance ~377 Ω), causing the pronounced back reflection of the incident MW radiation without entering into the material. The calculated reflection losses for $BaTiO_3$/NBR rubber composite samples are shown in Figures 6.9(c) – (f) for different thicknesses. The two absorption peaks R_1 and R_2 are observed in 8-12 GHz and 15-18 GHz frequency range, respectively for all these composite samples. For example, the maximum R.L values observed are ~4 dB (R_1) at 10.4 GHz and ~7 dB (R_2) at ~17 GHz for ~10 mm thick MWAR50 composite sample. Similarly, MWAR60 samples showed R.L values ~6 dB (R_1) at ~9.9 GHz and ~10 dB (R_2) at 16.2 GHz for ~9 mm thick composite sample. Further, increasing the $BaTiO_3$ loading fraction in NBR (MWAR70), the maximum R.L values observed are ~7 dB (R_1) at 9.8 GHz and ~11dB R_2 at 16.5 GHz for thickness ~ 8 mm and for MWAR80, the maximum R.L values are at ~9 dB (R_1) at 9.5 GHz and ~18 dB (R_2) at 16.5 GHz at relatively lower thickness ~6.5 mm with respect to lower $BaTiO_3$ loading fraction composite samples. The significant enhancement of R.L. values in MWAR80 samples, particularly absorption associated with R_2 is due to the higher effective loading of $BaTiO_3$ powder i.e. four fold as compared to MWAR50 sample.

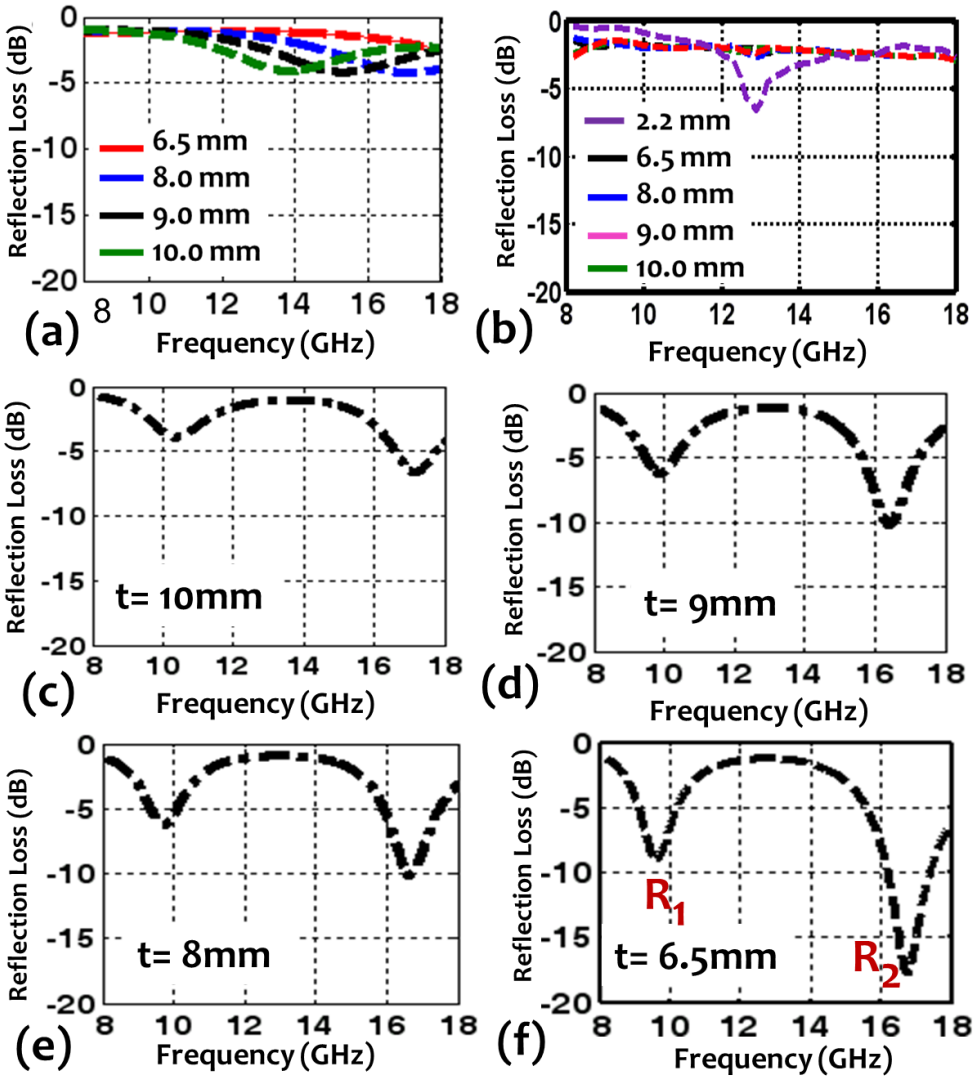

Figure 6.9 : Calculated R.L. plots for $BaTiO_3$/NBR composites over 8-18 GHz for (a) Pure NBR sheet (b) Pure $BaTiO_3$ powder sample and $BaTiO_3$ powder rubber composite samples with filler loading of (c) 50 wt% (d) 60 wt% (e) 70 wt% (f) 80 wt%

These results suggest that higher R.L. can be achieved at reduced thickness by increasing the effective $BaTiO_3$ loading fraction. In addition, the thickness of these absorbers also depend on material's parameter and should be in the order of $\sim\lambda/\sqrt{\varepsilon'\mu'}$ to realize impedance matching for enhanced MW absorption [Petrov and Gagulin, 2001] Thus, the observed large materials effective dielectric constant of MWAR80 $BaTiO_3$/NBR composites has resulted into reduced absorber thickness as compared to the other $BaTiO_3$/NBR composite samples.

To understand the appearance of the double absorption peaks R_1 and R_2, theoretical simulation has been carried out for MWAR80 composition for different sheet thicknesses and results are shown in Figure 6.10(a). The observed frequency difference ΔR (= $R_2 - R_1$) ~7 GHz is found to be constant and nearly insensitive to the absorber sheet thickness. This suggests that the origin of this second absorption peak R_2 is due to the second order dipolar resonance, appearing within the investigated frequency window. Moreover, the first absorption peak R_1 is because of the dipolar relaxation during incident EM interaction with the existing dipoles in $BaTiO_3$ material. In spite of thickness insensitive ΔR, Reflection Loss amplitude shows thickness dependence, as can be seen in Figure 6.10(a). Thus, optimal $BaTiO_3$ loading in NBR may provide efficient microwave absorption with reduced thickness in the desired 8-18 GHz frequency range.

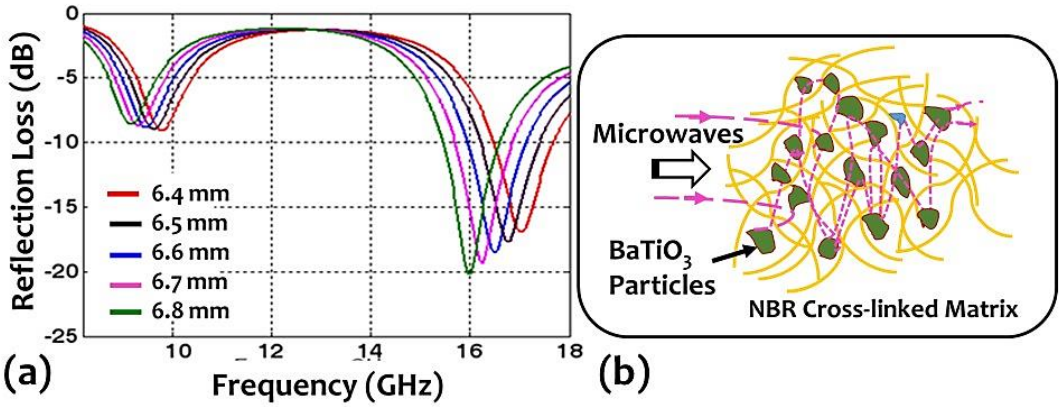

Figure 6.10 : Thickness dependent reflection loss profile for 80 wt% loaded rubber composite (b) Schematic for possible microwave absorption in rubber composites.

In composites, not only dipolar relaxation within the ferroelectric particles is responsible, but also the presence of multiple scattering sites due to in-homogeneous size and shapes of $BaTiO_3$ particulates in the host matrix, are causing the MW absorption. Considering the same, a possible mechanism for microwave interaction is shown in a schematic given in Figure 6.10(b) for $BaTiO_3$ impregnated NBR composites. $BaTiO_3$ particles are well dispersed during the optimized processing of material during fabrication of composite samples. This well dispersion of $BaTiO_3$ particles within the rubber matrix is responsible for the maximum scattering within medium and thus leading to the enhanced MW absorption for the composite systems [Kong *et al.*, 2014]. Further, this multiple scattering in the composite samples eventually leads to the enhanced entrapment of incident electromagnetic energy due to the larger interaction of microwaves with electric dipoles in $BaTiO_3$ material. These multiple scattering events also depend on the concentration of $BaTiO_3$ filler particles in the rubber matrix and thus an optimized concentration is desired to realize the effective MW absorption. The present investigations suggest the optimal loading of $BaTiO_3$ particles in rubber matrix to achieve the maximum R.L values in 8-18 GHz, at reduced sheet thicknesses.

6.3 DEVELOPMENT OF BISMUTH FERRITE ($BiFeO_3$) MULTIFERROICS AND ITS RUBBER COMPOSITES

The $BiFeO_3$ (BFO) perovskite oxide has been extensively studied for its multiferroic properties due to the simultaneous presence of ferroelectricity with high Curie temperature (T_c ~ 1100 K) and G-type antiferromagnetic ordering with high Neel temperature (T_N ~ 640K) [Teague *et al.*, 1970; Fischer *et al.*, 1980]. At room temperature, BFO is a distorted rhombohedral crystal structure with lattice parameters $(a=b=c)_{rh}$=3.965 A° and α = 89.3 – 89.48° and arranged in R3c space group symmetry, as shown in Figure 6.11 [Palewicza *et al.*, 2010].The Bi^{3+} cations are placed at eightfold coordinated corner sites of a cubical unit and Fe^{3+} at the center of cubical structure within the cage of oxygen octahedron. In the R3c arrangement, two cubic BFO unit cells are settled in such a way that relative displacement of cations with respect to O^{2-} anions, is in [111] direction. However, both oxygen octahedrons present in the structure are rotated around <111> axis in opposite directions [Kubel and Schmid, 1990]. The distortion in the rhombohedral structure is due to non-centrosymmetric displacement of Bi^{3+} and Fe^{3+} ions, leading to the ferroelectric polarization in BFO along $[111]_{pseudocubic}$ [Wang *et al.*, 2003]. Further, the asymmetric charge distribution at Bi^{3+} and Fe^{3+} sites and Fe^{2+}/Fe^{3+} charge hopping in BFO are responsible for poor dielectric/electric properties [Li *et al.*, 2015]. The short-range magnetic ordering in BFO is governed by Fe^{3+} spins situated in the vicinity of 6 nearest Fe antiparallel spins. However, a weak spin canting has been observed in BFO due to the magneto-electric coupling of spin cycloid with polarization vector, resulting into the weak room temperature magnetization [Lebeugle *et al.*,

2008; Catalan and Scott, 2009]. As the periodicity of corresponding spin cycloid is ~62 nm, the weak magnetization only appears at the nanometric regime in BFO [Wang *et al.*, 2004].

The recently observed large magnetic, ferroelectric and magneto-electric properties of BFO attracted attention exploring the possible applications such as four state memory devices, voltage controlled magnetic sensors etc.. There are very few studies on MW absorption properties for this material. The large ferroelectric polarization and magneto-electric coupling in BFO may show enhanced MW absorption in the extended frequency window. In spite of these advantages, there are numerous issues and challenges with BFO material system, especially the synthesis of phase pure material, and leakage current, which ultimately affect the material's performance. The existence of impurity/residual phases viz. Bi_2O_3, $Bi_2Fe_4O_9$, $Bi_{25}FeO_{40}$ etc. may limit drastically the MW absorption properties of BFO system [Mazumder *et al.* 2007]. Efforts have been made to obtain pure phase BFO material by the sol-gel process [Jia *et al.*, 2009], solid state route [Pandey and Singh, 2009], chemical co-precipitation [Chen and Wua, 2007], hydrothermal synthesis [Lu *et al.*, 2007] etc. In the present chapter, we have optimized synthesis process for nanocrystalline phase pure BFO powder by modulating the pre and post synthesis heat treatment conditions to get phase pure material.

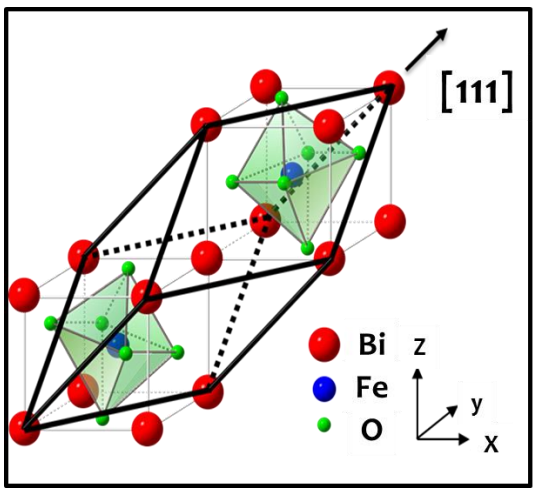

Figure 6.11 : (a) R3c crystal arrangement of BFO multiferroics [Source: Shima *et al.*, 2013]

6.3.1 Experimental Procedure

$BiFeO_3$ samples are prepared using sol-gel synthesis technique. The process steps for the preparation of $BiFeO_3$ are shown in schematic block diagram (Figure 6.12). In the first step, dissolution of glycine was carried out in 50 ml ethanol solution. After the homogeneous mixing of glycine (3.38g) in 50 ml ethanol, the stoichiometric equimolar ratio of bismuth nitrate $Bi(NO_3).5H_2O$ (10.91g) and iron nitrate $Fe(NO_3).9H_2O$ (9.09g) are dissolved in glycinated ethanol solution and a small amount of nitric acid (~5 ml) was added to dissolve chemical reagents completely. The dissolved mixture was homogenized in magnetic stirring for 20 minutes and 5 ml of H_2O_2 solution was added in the reaction mixture.

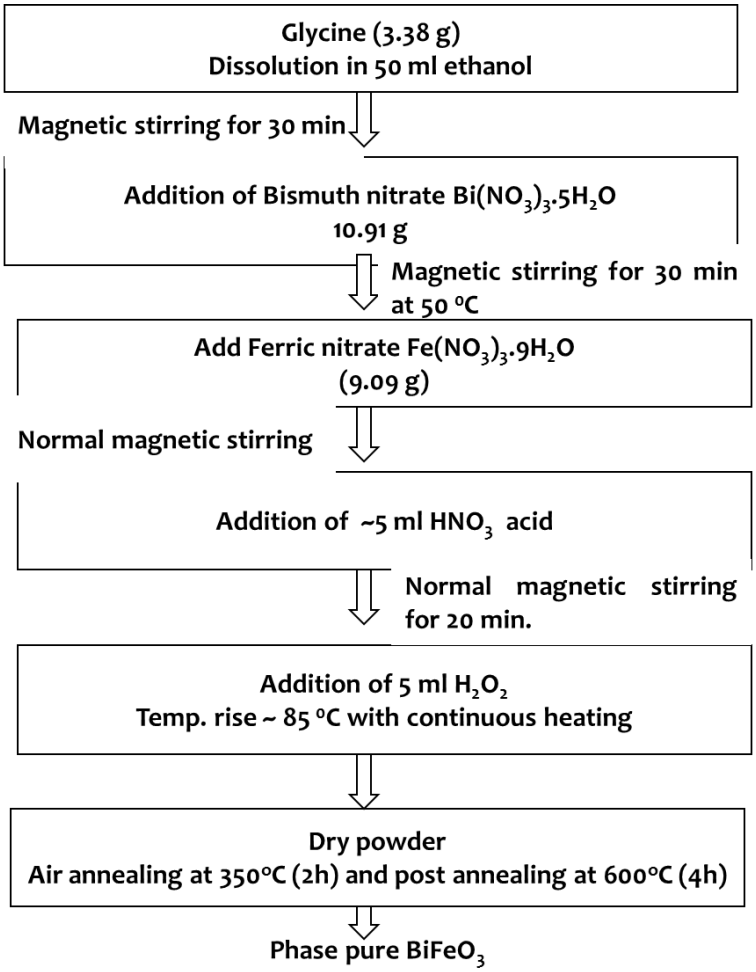

Figure 6.12 : Process flow chart for synthesis of BFO nanocrystalline powder

The resultant mixture was heated at ~85°C for the removal of residual solvent. The brown color powder was collected after this combustion, process ground and annealed at 350°C for 2h in ambient conditions. The BFO powder sample was further post-annealed for a longer duration of 4h at 600°C to get the desired crystallinity in the materials. The synthesized material was characterized using different structural, micro-structural, optical and microwave characterization techniques to understand the structure-property correlation for MW absorption in BFO material. The BFO powder annealed at 600°C for 4h was used as filler material for fabricating the rubber based composites using rubber processing units viz. Two Roll Mixing Mill (TRMM) and High-Temperature Compression and Moulding Press (HTCMP), as discussed earlier. A series of rubber based absorbers were prepared as mentioned in Table 6.2, for understanding the microwave absorption properties in BFO-rubber composite samples

Table 6.2: List of rubber composites loaded with BFO powder annealed at 600°C for 4h duration

S. No.	Sample Code	Quantity of NBR (g)	Wt% of BFO in compound	Quantity of BFO Powder (g)	Enhancement in filler loading as compared to sample BFR50 (x)
1	BFR50	50	50	50	1
2	BFR60	50	60	75	1.5
3	BFR70	50	70	116.7	2.33
4	BFR80	50	80	200	4

6.3.2 Results and Discussion

6.3.2.1 X-ray Diffraction Analysis

The XRD spectra of BFO powder samples annealed at 350°C for 2h and sequentially post annealed at 600°C for 4h, are shown in Figure 6.13. The observed XRD spectra confirm the formation of rhombohedral structure (R3c) in both the annealed samples, which is consistent with reported literature [Hu *et al*., 2011]. However, 350°C annealed sample has additional diffraction peak corresponding to impurity phase of Bi_2O_3 at 2θ ~28°, which vanished with further annealing of powder at 600°C for longer duration. Further, enhancement in $BiFeO_3$ rhombohedral peaks intensity at higher annealing temperature of 600°C, indicating the better crystallinity in the sample. The average crystalline size of this BFO sample, estimated using Debye-Scherer formula is ~50 nm.

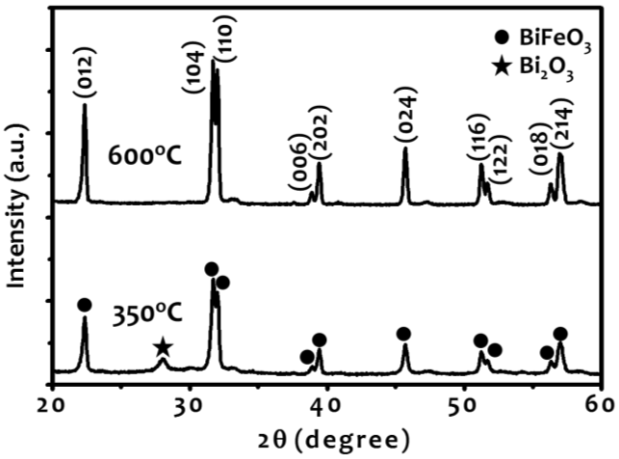

Figure 6.13 : XRD spectra of BFO powders sample annealed at 350°C (2h) and 600°C (4h)

6.3.2.2 FTIR Studies

Fourier Transform Infrared Spectroscopy (FTIR) spectra for BFO sample annealed at 600°C for 4h is shown in Figure 6.14. The observed vibrational modes at ~ 550 cm^{-1} and 438 cm^{-1} (Inset Fig. 6.14), are the characteristics vibrational modes for rhombohedral $BiFeO_3$ material. The broad absorption mode at ~ 438 cm^{-1} is attributed to bending of Fe – O bond in the FeO_6 octahedral unit and also due to the BiO_6 octahedral unit that exhibits an IR vibrational mode ~ 450 cm^{-1}. The broad vibrational mode centered at ~ 550 cm^{-1} also corresponds to Fe-O stretching vibrational mode, present in FeO_6 octahedral unit. The lack of any organic or impurity modes in FTIR spectrograph confirms the purity of the synthesized material.

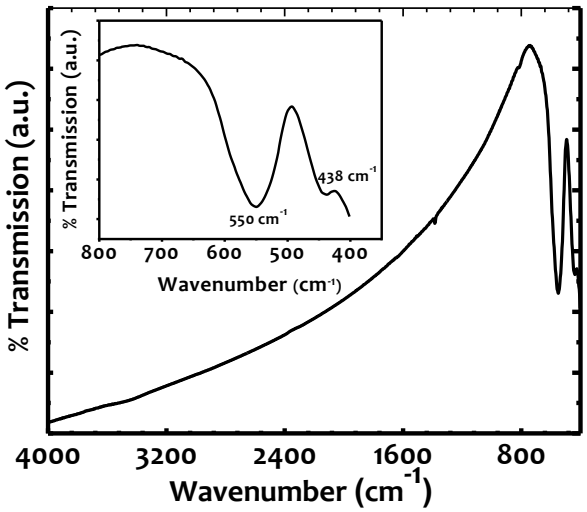

Figure 6.14 : FTIR spectra of BFO post annealed powder sample at 600°C for 4h

6.3.2.3 Morphological Characterization

The scanning electron micrographs for pristine and post annealed $BiFeO_3$ samples are shown in Figure 6.15. The pristine $BiFeO_3$ sample, exhibits a random distribution of agglomerated particles, whereas the post-annealed sample shows well-textured microcubes of $BiFeO_3$ material. This image indicates that the post-annealing treatment provides conversion of randomly oriented grains into larger microcubes. The surface texturing of multiferroic $BiFeO_3$ materials may be important for enhanced microwave absorption in the desired frequency range. The EDX spectra, as shown in Figure 6.15(c), confirms the presence of Bi, Fe and O elements in a stoichiometric ratio.

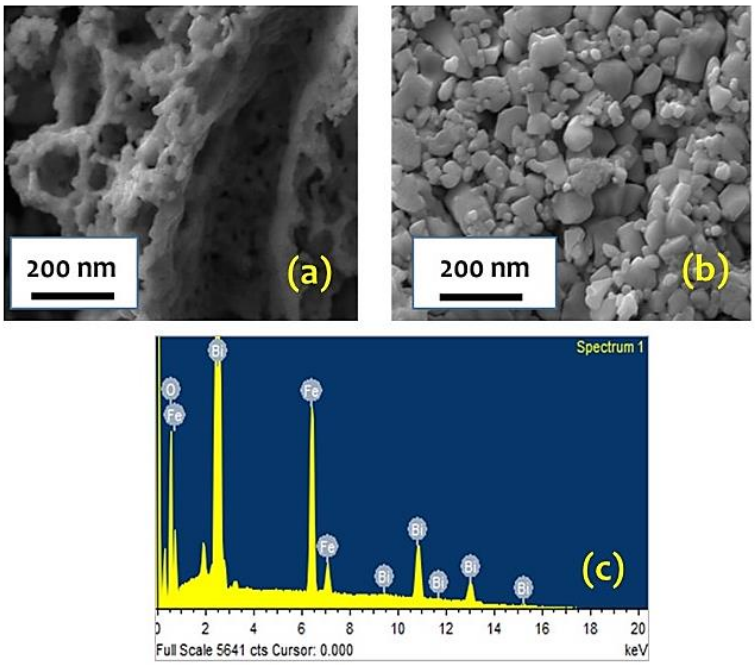

Figure 6.15 : SEM micrograph for (a) 350°C annealed sample (b) Post annealed sample at 600°C for 4h (c) Corresponding EDX spectra

6.3.2.5 Magnetic Studies

The room temperature M-H curve is shown in Figure 6.16 for 600°C (4h) annealed BFO powder sample. The weak ferromagnetic behavior can be inferred in combination with linear unsaturated behavior. The observed results are consistent with some of the reported literature [Wei and Xue, 2008; Huang *et al.*, 2013]. The room temperature magnetization is ~ 0.15 emu/g for this BFO sample. Further, the magnetization is un-saturated even at relatively large magnetic fields up to 1.5T. This weak ferromagnetism may be due to non-collinear/canted spin arrangements of iron in BFO crystal lattice. The reduction of particle size below ~62 nm in these samples has resulted into the breaking of long-range antiferromagnetic ordering and causing the observed ferromagnetic behavior in conjunction with uncompensated surface spins, leading to further enhancement in the net magnetization of BFO nanoparticles [Jia *et al.*, 2009; Dormann and Nogues, 1990]. Moreover, anisotropies in these BFO nanoparticles due to lattice strain may also modify the magnetic properties. Further, the observed coercive field (H_c) for the BFO sample is ~180 Oe, as shown in the inset of Figure 6.16.

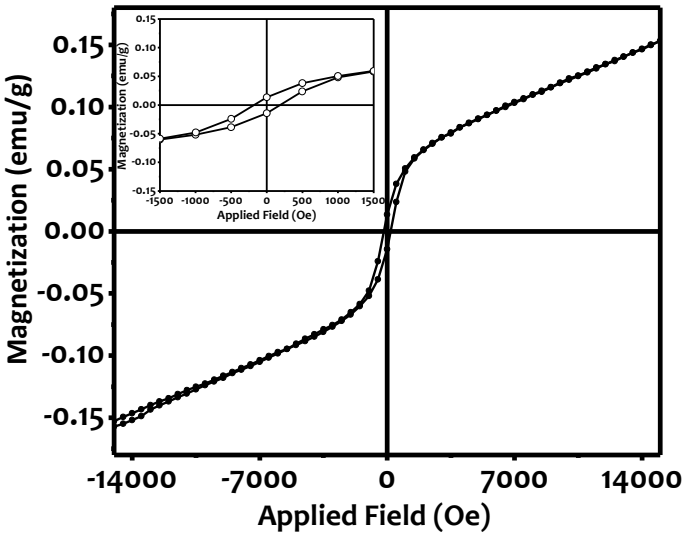

Figure 6.16 : Room temperature M-H curves for BFO sample annealed at 600°C for 4h duration

6.3.2.6 Microwave Studies

The frequency dependent complex permittivity plots are shown in Figure 6.17(a). The real permittivity (ε_r') values are found ~ 45±4 in 8-18 GHz frequency range and are nearly constant with very little dispersion over the entire frequency range. The observed ε_r' values are found comparatively higher than earlier reported values by Zhong *et al.* [Zhong *et al.,* 2016]. The imaginary permittivity (ε_r'') values are found in the range of ~ -15 to -22 over 8-18 GHz frequency range as shown in Figure 6.17(a). The dielectric loss tangent ($\tan\delta_e$) for the BFO powder has been calculated and plotted in Figure 6.16(b). The measured $\tan\delta_e$ values show a small increase in magnitude from ~ -0.35 to -0.50 with frequency. The real (μ_r') and imaginary permeability (μ_r'') values for BFO powder observed ~1.0 and ~ -0.02, respectively, over the entire frequency range. The synthesized powder does not show any significant magnetic loss in the investigated frequency range and therefore not plotted here.

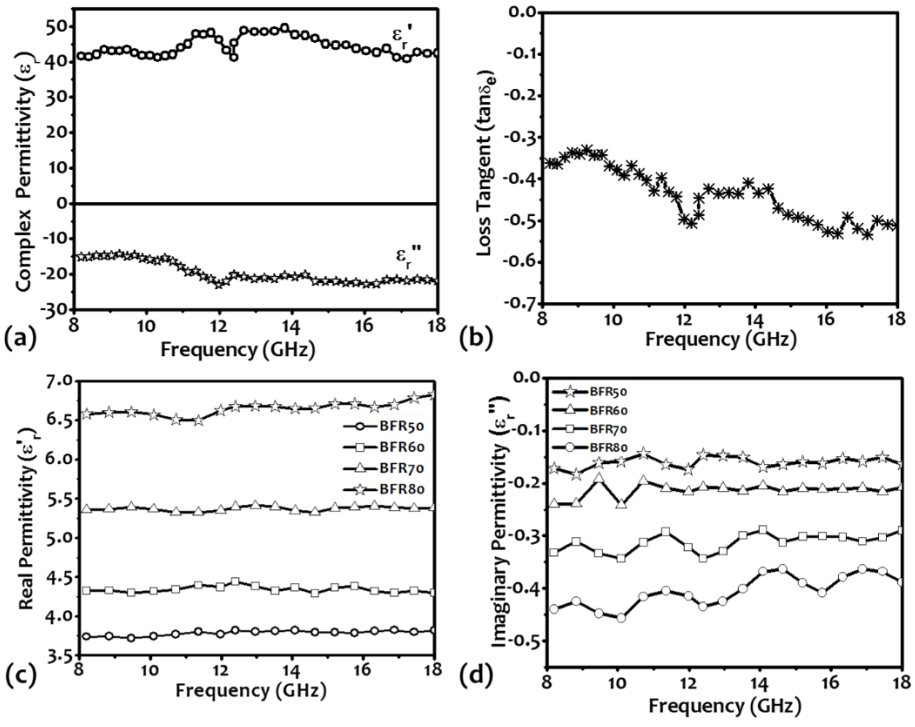

Figure 6.17 : (a) Complex permittivity plots for 600°C annealed BFO powders over 8-18 GHz frequency range (b) Dielectric loss tangent ($\tan\delta_e$) plot for respective powder sample (c) Real permittivity plots for BFO powder loaded rubber composites (d) Imaginary permittivity plots for respective rubber composites

The frequency dependent real permittivity plots of BFO loaded rubber composites with different filler concentration (BFR50-BFR80) are shown in Figure 6.17(c). These ε_r' values are ~ 3.8, ~ 4.3, ~ 5.3 and ~ 6.7 for BFR50, BFR60, BFR70 and BFR80 rubber composites respectively, showing nearly non-dispersive characteristics in 8-18 GHz frequency range. The enhancement in ε_r' values with filler concentration is attributed to the effective permittivity contribution of BFO functional material in the rubber composition. Similarly, ε_r'' values for rubber composites also increased with increasing the filler concentration and values ~ -0.15, ~ - 0.20, ~ -0.30 and ~ -0.40 for BFR50, BFR60, BFR70 and BFR80 rubber composites respectively, with very small dispersion characteristics in 8-18 GHz frequency range shown in Figure 6.17(d). The contribution of $\varepsilon_r'' \approx \sigma/(2\pi f\varepsilon_o)$ is highly dependent on conductivity(σ) of filler materials in the insulating medium. The observed high values of ε_r'' in these BFO-rubber composite samples are attributed to onset of ohmic connections and nano-capacitance in intra-atomic BFO nanostructures within rubber matrix [Jiang *et al*., 2015].

The reflection loss (R.L.) were calculated, using Eq.(4.2) as discussed earlier, using measured complex permittivity and permittivity values of these BFO-rubber composites for different thicknesses. The results are summarized in Figures 6.18(a)-(d). Interestingly, the R.L. plots show dual band resonance behavior for all these BFO-rubber composite samples, similar to that of $BaTiO_3$ loaded composites discussed earlier in this chapter. For BFR50 composite, first resonance peak (R_1) is observed at ~9.5 GHz with R.L. value ~5 dB in conjunction with the second order resonance peak (R_2) observed at 16 GHz with R.L. value ~10 dB for 11 mm thick sheet. The positions of these resonance peaks are almost similar to that of MWAR50 composite sample. In the case of higher loading of filler (BFR60), R_1 and R_2 peak absorption values enhanced to ~6 dB and ~13 dB, respectively at lower absorber thickness ~10 mm. With further increase in BFO loading fraction (BFR70), the resonance peak absorption values have increased up to ~7 dB and ~15 dB, respectively for reduced absorber thickness ~9 mm.

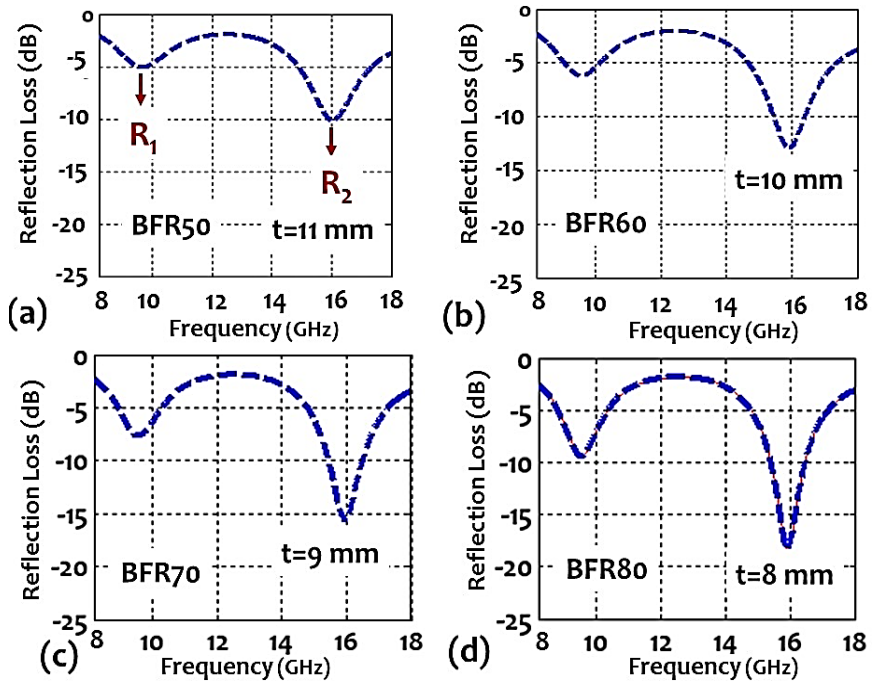

Figure 6.18 : Calculated R.L. plots for BFO/NBR composites over 8-18 GHz for rubber composite samples with filler loading of (a) 50 wt% (b) 60 wt% (c) 70 wt% (d) 80 wt%

In the case of maximum BFO loading fraction (BFR80), the peak absorption values have increased to found ~9 dB and ~18 dB at 9.5 GHz (R_1) and 16 GHz (R_2), respectively, at the lowest absorber thickness ~8 mm among the different BFO-rubber composite samples. For this particular sample, the observed R.L. values corresponding to R_1 and R_2 are identical to $BaTiO_3$ based absorber having same filler loading (MWAR80). These studies indicate that with an increase in

filler loading, the absorber thickness can be reduced with enhanced R.L. value of R_1 and R_2 resonance peaks as observed in the case of $BaTiO_3$, discussed in the previous section. However, the absorber thickness on BFO-rubber is relatively much larger in comparison to $BaTiO_3$-rubber composite sample due to relatively lesser ferroelectric characteristics in BFO bulk sample (~ 6.1 $\mu C/cm^2$) [Teague *et al*., 1970] in comparison to $BaTiO_3$ (~25 $\mu C/cm^2$) [Phule and Risbud, 1991]

Figure 6.19 shows the thickness dependence of R.L. profile for BFR80 rubber composite sample in the range of 7.6-8.2 mm. The observations suggest that both R_1 and R_2 dual resonance characteristics shift towards lower frequency side, with ΔR (= R_2 – R_1) values found almost constant ~7 GHz, with increasing the thickness of the composite sheet. This is similar to observations made in $BaTiO_3$ based rubber composite MWAR80. These observations in conjunction with measured relative permeability values confirm that the major contribution in reflection loss characteristics is because of the ferroelectric properties of multiferroic $BiFeO_3$, whereas weak magnetization in this system has no significant role in MW absorption.

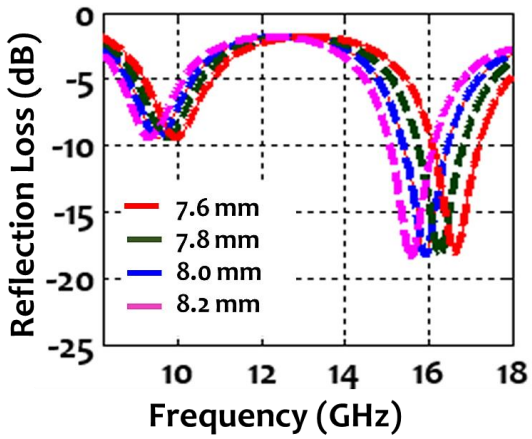

Figure 6.19 : Thickness dependent R.L. profile for BFR80 rubber composite

6.4 CONCLUDING REMARKS

In conclusion, phase pure tetragonal $BaTiO_3$ bulk samples have been synthesized by using simple and cost effective solid state process. Formation of phase pure tetragonal $BaTiO_3$ has been investigated from XRD and Raman spectra. The 1100°C annealed $BaTiO_3$ sample with maximum tetragonality showed the highest values of dielectric loss tangent ($\tan\delta_e$) > 0.4 over the entire frequency range 10-18 GHz of interest. These studies suggest that $BaTiO_3$ material may be a good choice as a filler in NBR for microwave absorption applications. The computed R.L. values of these $BaTiO_3$/NBR composites showed two prominent absorption peaks (R_1 & R_2) in the frequency range 8-18 GHz. The 80wt% loaded $BaTiO_3$-rubber composite sample showed the best R.L. values ~9 dB at 9.5 GHz and ~18 dB at 16.5 GHz for ~6.5 mm sheets, explaining the observed dual band resonance in such composites. The onset of this dual band is attributed to the ferroelectric induced dipolar relaxation at 9.5 GHz and its second order resonance at 16.5 GHz in such composite systems. Further, multiferroic nanostructured $BiFeO_3$ powder has been synthesized using simple, scalable and reproducible sol-gel route. The annealing conditions are optimized for rhombohedral (space group R3c) phase pure powder. Elastomeric rubber composites are prepared by dispersing the $BiFeO_3$ with different filler ratio for MW absorption applications. These materials also show almost similar MW behavior as observed for $BaTiO_3$ based rubber composites. These observations for BFO and BTO rubber composites confirm the contribution of ferroelectric domains present in BFO/BTO for MW absorption, suggesting that this dual resonance may be a generic feature in ferroelectric based MW absorber systems.

...